applied sciences

MDPI

Article

A Methodology for the Mechanical Design of Pneumatic Joints Using Artificial Neural Networks

Michele Gabrio Antonelli [1], Pierluigi Beomonte Zobel [1], Enrico Mattei [2] and Nicola Stampone [1,*]

[1] Department of Industrial and Information Engineering and Economy (DIIIE), University of L'Aquila, P. le Pontieri 1, Località Monteluco, 67100 L'Aquila, Italy; gabrio.antonelli@univaq.it (M.G.A.); pierluigi.zobel@univaq.it (P.B.Z.)

[2] Department of Information Engineering, Computer Science and Mathematics (DISIM), University of L'Aquila, Via Vetoio, 67100 L'Aquila, Italy; enrico.mattei@graduate.univaq.it

* Correspondence: nicola.stampone@graduate.univaq.it

Abstract: The advent of collaborative and soft robotics has reduced the mandatory adoption of safety barriers, pushing human–robot interaction to previously unreachable levels. Due to their reciprocal advantages, integrating these technologies can maximize a device's performance. However, simplifying assumptions or elementary geometries are often required due to non-linear factors that identify analytical models for designing soft pneumatic actuators for collaborative and soft robotics. Over time, various approaches have been employed to overcome these issues, including finite element analysis, response surface methodology (RSM), and machine learning (ML) algorithms. Based on the latter, in this study, the bending behavior of an externally reinforced soft pneumatic actuator was characterized by the changing geometric and functional parameters, realizing a Bend dataset. This was used to train 14 regression algorithms, and the Bilayered neural network (BNN) was the best. Three different external reinforcements, excluded for the realization of the dataset, were tested by comparing the predicted and experimental bending angles. The BNN demonstrated significantly lower error than that obtained by RSM, validating the methodology and highlighting how ML techniques can advance the prediction and mechanical design of soft pneumatic actuators.

Keywords: soft robotics; soft pneumatic actuator; external reinforcement; mechanical design; artificial neural network

Citation: Antonelli, M.G.; Beomonte Zobel, P.; Mattei, E.; Stampone, N. A Methodology for the Mechanical Design of Pneumatic Joints Using Artificial Neural Networks. *Appl. Sci.* **2024**, *14*, 8324. https://doi.org/10.3390/app14188324

Academic Editor: Rui Araújo

Received: 2 August 2024
Revised: 2 September 2024
Accepted: 11 September 2024
Published: 15 September 2024

1. Introduction

In recent decades, in the field of robotics, human–machine interaction has increased with both the advent of collaborative robotics [1] and soft robotics [2]. Robots are now allowed to operate in shared workspaces with operators [3,4], eliminating the need for dedicated spaces with safety barriers. Indeed, human–machine interaction has been extended into confined spaces [5] with, for example, path planning [6,7] and emotional intelligence [8] algorithms. This extends the adaptability of robots even in unstructured environments, as it endows robots with unexpected capabilities compared to the past through high degrees of freedom, such as stretching [9], bending [10,11], twisting [12], locomotion [13–15], jumping [16], swimming [17], climbing [18], and growing [19]. This is possible using silicone rubbers [20], which allow for soft and easily deformable actuators. The integration of these technologies can maximize the performance of a device, thanks to the integration of the advantages of each technology. For instance, utilizing the benefits mentioned for cobots equipped with soft end-effectors enables the manipulation of delicate objects with extreme dexterity and security [21–23].

Several types of actuations have been proposed over the years [24], but the pneumatic one is the most adopted [25]. Indeed, it enables actuators to be made lightweight, safe,

inexpensive, easy to manage, and with a high power-to-weight ratio. Actuators of this type are known as soft pneumatic actuators (SPAs), and can be used without [26] or with an external [27] or internal [13] reinforcement to limit and guide their deformation.

On the other hand, there are several disadvantages involving the complex identification of analytical models [28,29] for designing SPAs, since they are affected by non-linearities due to air compressibility, silicone rubbers' viscoelastic behavior, hysteresis [30,31], friction [32] between silicone and reinforcement when used, and large deformations. Over the years, analytical models have been formulated to describe the behavior of SPAs [33]. Models are often complex and require the identification of parameters. In addition, simplifying assumptions must usually be made or simple geometries must be used to describe and predict the actuator behavior.

An approach for achieving a predictive model for SPAs is response surface methodology (RSM) [34,35]. Firstly, it allows the planning of testing campaigns to minimize the resources used and the time required by identifying a predictive polynomial model of the analyzed response (e.g., bending angles of the SPA) based on the input parameters (geometric or functional parameters of the SPA) [36,37]. Secondly, it aims to simplify complex analytical models that have already been identified: several simulations of an identified model are run, and with regression methods, the responses fit simpler models.

Alternatively, static finite element analysis (FEAs), i.e., simulations with constant and uniform application of pressure to surfaces [13] or transient [38] with fluid–structure interaction, can be employed to predict SPA behavior. However, simulations are computationally expensive and time-consuming for numerical resolution. Integration between FEAs and RSM is helpful to minimize the number of simulations needed to characterize SPAs [39].

A data-driven approach involves machine learning algorithms that correlate input data (independent variables) with output data (dependent variable) without adopting simplifying assumptions for modeling the actuator. Artificial neural networks (ANNs) have been implemented to describe the workspace of SPAs [40–42]. In addition, ANNs can also control an SPA by continuously learning [43]. Approaches between FEAs and ANNs adopt data for training that are derived directly from the numerical results of simulations [44]. Alternatively, the accuracy of ANN predictions can be improved with a hybrid approach between model-free and an analytical model, called a physics-informed recurrent neural network [45]. An integration approach between ANNs and fuzzy logic, known as fuzzy neural networks, allows the replacement of the neural network pretraining with knowledge-based fuzzy logic [46]. Another work [47] shows how the control performance improves with a fuzzy neural network sliding control, even when expanding the actuation range to 4.0 bar. Finally, it is possible to control an SPA with four chambers by the predictions of an ANN and fuzzy logic methodology to integrate several position controllers into one valid control over the whole range [48].

In this work, the presented SPA consists of an inner tube made of hyper-elastic silicone rubber, an external reinforcement in thermoplastic polyurethane (TPU), and a polylactic acid (PLA) connector. A Bend dataset was created to train different regression algorithms. In this dataset, responses regarding bending angles as a function of geometric parameters of the reinforcement and feeding pressure are reported. The Bilayered neural network (BNN) was the best model, resulting in the smallest error in both training and validation. Hence, to validate the methodology, the BNN was adopted for the mechanical design of joints of three external reinforcements, which had not previously been adopted to create the Bend dataset.

The mechanical design of the SPA, adopting the ML approach, and creating a proper dataset based on experimental tests represent the novelty of the work. The following items represent the main contents of the work:

- The realization of the Bend dataset;
- The adoption of the ML to train 14 regression algorithms on the dataset;

- The identification of the best algorithm for the mechanical design of the proposed SPA;
- The experimental test of the methodology on three tubes and reinforcements that differ in the joints' length, mass, geometric, and functional parameters.

The paper is organized as follows. Section 2 describes the rationale and the realization of the SPA. Section 3 explains the testing campaign to realize the Bend dataset and the training phase to identify the best regression algorithm. Experimental testing of the methodology is analyzed in Section 4. Sections 5 and 6 present a discussion and the conclusions, respectively.

2. Materials and Manufacturing Process

2.1. Rationale of the SPA

The rationale of the SPA is detailed in a preliminary work [36]. The SPA consists of an inner tube, an external reinforcement, and a connector. The reinforcement contains the radial deformation and guides, by cuts, the deformation of the actuator when pressurized. Figure 1a details the cuts made on the external reinforcement to create geometric asymmetries between the two sides of the SPA. This results in an asymmetry in bending stiffness due to an inextensible layer (the part of the external reinforcement not involved in the cuts). The actuator bends toward the side with greater stiffness, as shown in Figure 1b. In addition, Figure 1c specifies how the single segment is characterized by an open sector (L_o) and a closed sector (L_c). The geometric parameters that define the reinforcement are the length of the segment (L), the ratio open—total (R), and the closing angle of the inextensible layer (Θ).

Thus, L is the sum of the open and closed sector length:

$$L = L_O + L_C \quad (1)$$

R is the ratio between the open sector and total segment length, following Equation (2).

$$R = \frac{L_O}{L} \quad (2)$$

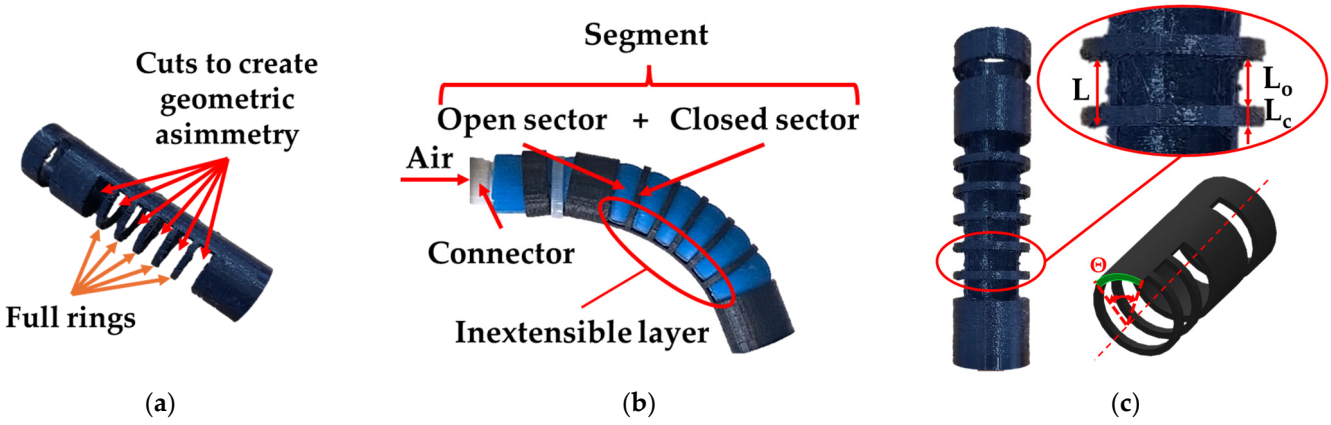

Figure 1. The adopted SPA: (**a**) external reinforcement with cuts to create geometric asymmetries; (**b**) example of SPA bending under pressurization toward the direction of the inextensible layer; (**c**) details of geometric parameters of the reinforcement, with green indicating the inextensible layer and red the closing angle.

2.2. Component Realization

The inner tube in silicone rubber R PRO20 (Reschimica, Barberino Tavarnelle, Italy) is made by injection molding after making the base–catalyst mixture in a 1:1 ratio and removing air bubbles, as in [36]. Its dimensions are the outer diameter, thickness, and tube

length of 24, 3, and 115 mm, respectively. One end is closed; the other houses the Polylactic acid (PLA) connector and shows a race to ensure the pneumatic and mechanical seal. Reinforcements made of TPU 95A (SUNLU, Hong Kong, China) were 3D-printed with the following parameters: printing speed of 40 mm/s; inner and outer wall speeds of 20 mm/s; extruder temperature of 220 °C; printing plate temperature of 65 °C; and filling percentage of 100% according to concentric configuration. All reinforcements have an outer diameter of 28 mm and a thickness of 2 mm. The only functional parameter is the feeding pressure, P. The variable geometric parameters of the reinforcement cuts are L, R, and Θ. Table 1 reports the chosen parameters and their ranges of variation.

Table 1. Functional and geometrical parameters with their ranges of variation.

Symbol	Name	Values	Unit
P	Feeding Pressure	0.0–1.2	(bar)
L	Segment Length	4.0–10.0	(mm)
R	Ratio Open—Total	0.25–0.75	-
Θ	Closing Angle	40–120	(°)

A total of twenty-seven external reinforcements, corresponding to the twenty-seven combinations of the geometric parameters shown in Table 2, were designed by a 3D CAD modeler and realized. Figure 2 shows the reinforcements after the 3D-printing process. All these prototypes have five closed sectors and consequently six open sectors. For each prototype, the same closed and open sectors are repeated five and six times, respectively. Bending is allowed by the open sectors alone, while the closed sectors contain the radial expansion of the inner tube.

Table 2. Values of the geometrical parameters for the twenty-seven external reinforcements.

Reinforcement	L (mm)	R (-)	Θ (°)	Reinforcement	L (mm)	R (-)	Θ (°)	Reinforcement	L (mm)	R (-)	Θ (°)
1	4	0.25	40	10	4	0.25	70	19	4	0.25	100
2	7	0.25	40	11	7	0.25	70	20	7	0.25	100
3	10	0.25	40	12	10	0.25	70	21	10	0.25	100
4	4	0.50	40	13	4	0.50	70	22	4	0.50	100
5	7	0.50	40	14	7	0.50	70	23	7	0.50	100
6	10	0.50	40	15	10	0.50	70	24	10	0.50	100
7	5	0.35	50	16	10	0.50	85	25	10	0.65	120
8	7	0.75	40	17	7	0.75	70	26	7	0.75	100
9	10	0.75	40	18	10	0.75	70	27	10	0.75	100

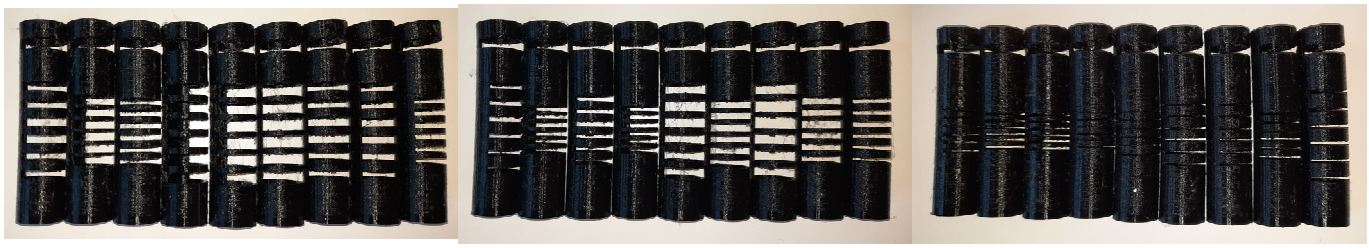

Figure 2. Prototypes with the geometric parameters in Table 2 after printing and support removal.

3. Dataset Construction and Regression Algorithms

3.1. Camera Calibration

Calibration of the camera employed was performed preliminary to the execution of the bending tests for the dataset creation. The RGB (Apple, Cupertino, CA, USA) camera used was an A2215 [49] with 12-megapixel resolution, 120° field of view, HD 1080p/60fps,

autofocus, and automatic image stabilization. The camera was set in a fixed position in front of the test bench where the actuator samples were placed. Fifteen images were imported into the Camera Calibration toolbox of MATLAB R2023b. In these images, the checkerboard (Figure 3a) with a characteristic dimension of 20 mm was shifted slightly to calibrate the camera and map the environment around it. In Figure 3b, there is the 3D reconstruction of the external world with the camera positioned at the point (0,0,0). In the same image, it is also possible to appreciate the position and orientation of the checkerboard in each of the images acquired and used in the calibration phase. Figure 3c shows the average error in pixels for each image adopted. The maximum error, shown by the solid red line, and the average error, in the orange dotted line, are 0.27 and 0.23 pixels, respectively, corresponding to 0.072 and 0.061 mm. This result was considered satisfying for the executed calibration. With these calibration parameters, it is possible to transform the coordinates of an image pixel into the respective X–Y coordinates and calculate the positions, displacements, and bending angles of the SPA.

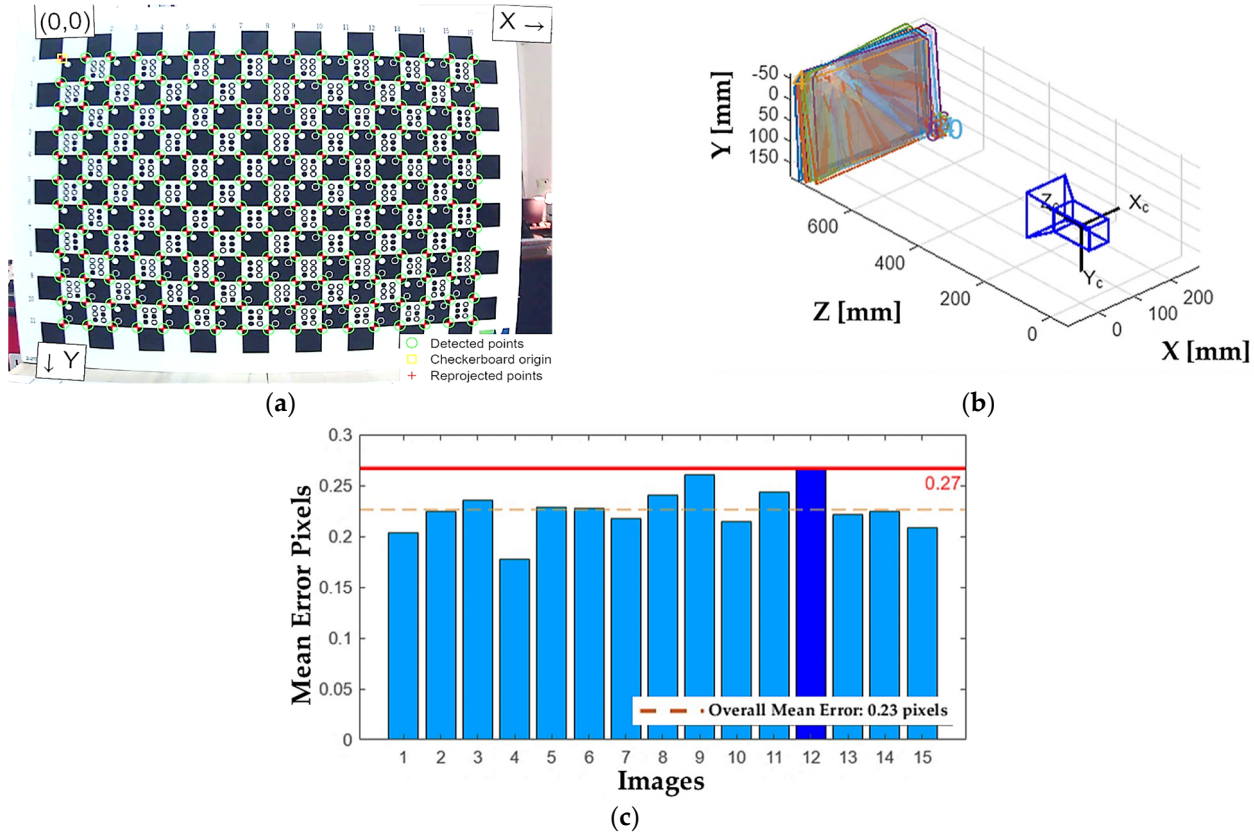

Figure 3. Camera calibration results: (**a**) the adopted checkerboard in one of the positions used for the camera calibration; (**b**) real-world 3D reconstruction with the camera positioned at the point (0,0,0); (**c**) mean errors of the fifteen images used in the calibration with the maximum error shown by the red solid line and the mean error the orange dotted line.

3.2. Bend Dataset

After calibration, a test campaign was carried out to build the Bend dataset. In each test, hereinafter called trial, there was a unique combination of the geometric and functional parameters of the external reinforcement. The twenty-seven external reinforcements were tested at seven different pressure levels for 189 tests and repeated three times, for an overall amount of 567 trials. In each of them, the average of the six bending angles of the open sectors, identified for the same parameter combination, was calculated. In the trials, the pressure was set with a precision regulator (SMC IR1220-N01-A, maximum pressure of 4.0 bar, SMC Corporation, Tokyo, Japan) and measured with a pressure

manometer (maximum pressure 2.5 bar, sensitivity 0.05 bar). The images were imported and processed in MATLAB R2023b. The parameters from the calibration results were used in the image analysis. The *undistorted* [50] and *imlocalbrighten* filters [51] can be used before identifying the bending angles of each test. The first filter rectifies errors induced by lens distortion; thus, the algorithm maps the coordinates of the undistorted output image to the input camera image using distortion coefficients. The second filter improves image contrast: a contrast adjustment realigns the image intensity values to the full display range of the data type. Thus, with an image with good contrast, which has more pronounced differences between black and white, it is easier to identify points of interest in image analysis.

Figure 4a shows the raw image acquired for reinforcement 6 at a pressure P of 1.2 bar, while Figure 4b and 4c show the same image with distortion correction and contrast enhancement, respectively. To better understand the influence of the filters, histograms of grayscale pixel intensities are shown in Figure 4d–f for each image. The differences that occurred by the application of the first filter are not appreciable to the naked eye. With histograms, it is possible to understand how the filter acts on the intensity of some pixels, correcting the distortion of the lenses. Furthermore, the minimal changes made during this correction justify the good results of the calibration. The second filter, on the other hand, marks contrast, especially in the darker areas of the image, as is evident from the reduction in the number of pixels in the low-intensity areas.

Finally, from the undistorted ImagePoints coordinates (in pixels) and calibration parameters, the *image2world2d* function was used to return the WorldPoints coordinates (X and Y in mm) by rigid transformation. Following this process, the dataset was available, and for each quatern of values of P, L, R, and Θ, there was given output bending angle of the open sector, α. In total, 189 combinations of four inputs were associated with the corresponding output bending angle.

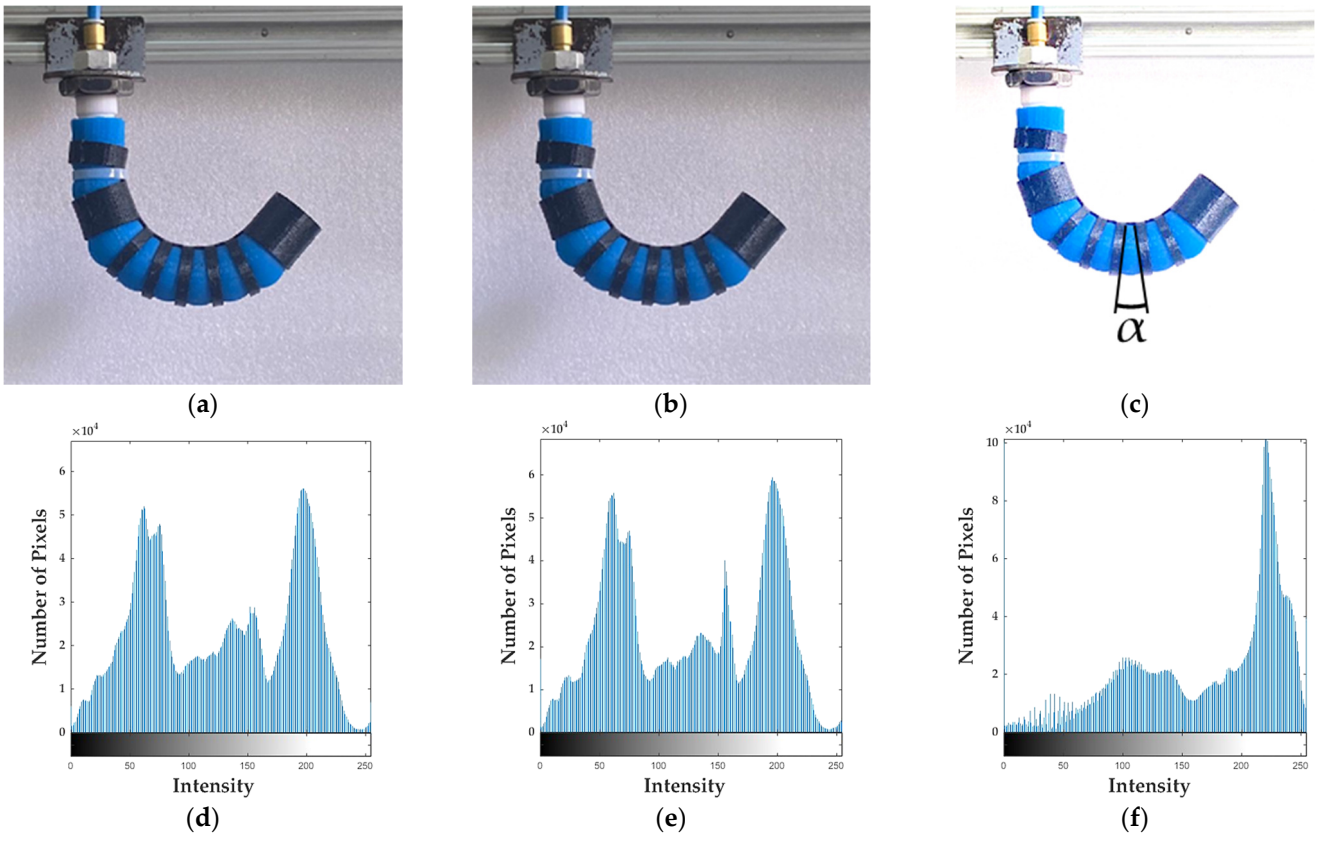

Figure 4. Example of test number 6, at P = 1.2 bar, L = 10 mm, R = 0.5, Θ = 40°: (**a**) raw image; (**b**) image after *undistorted* filter application; (**c**) image after *imlocalbright* filter application and detail

about open sector bending angle α. Histogram of pixel intensities for: (**d**) raw image; (**e**) undistorted image; (**f**) image with contrast improved.

3.3. Regression Algorithms

After creating the Bend dataset, the trials were divided 80% into training and 20% into validation [52]. Next, with the Regression Learner toolbox in MATLAB R2023b, inputs and outputs were normalized in the range 0–1 and set to analyze the performance of 14 regression algorithms. The results of root mean square error (RMSE) for the training and validation phases, training time, and model size are shown in Table 3. RMSE is defined as the standard deviation of the residuals, according to Equation (3):

$$RMSE = \sqrt{\sum_{i=1}^{n} \frac{\left(\alpha_{exp} - \alpha_{pre}\right)^2}{n}} \quad (3)$$

where α_{exp} and α_{pre} are the experimental and predicted responses, while n is the number of observations. The square elevation of the residuals prevents positive and negative values from canceling each other out. In addition, with this parameter, errors of greater value are amplified; therefore, they allow methods involving more significant errors to be discarded. Ideally, an RMSE value of 0 indicates a perfect fit between the measured response and that predicted by the algorithm.

Table 3. Performance results for different regression algorithms.

Algorithm	Training RMSE (°)	Validation RMSE (°)	Training Time (s)	Model Size (kB)
Coarse Tree	3.84	3.35	10.90	3
Medium Tree	2.68	1.84	12.05	4
Fine Tree	2.12	2.51	13.34	8
Linear SVM	2.50	1.99	8.89	8
Quadratic SVM	1.48	1.37	7.37	6
Cubic SVM	1.38	1.22	6.79	6
Medium Gaussian SVM	1.62	1.35	25.31	6
Coarse Gaussian SVM	2.44	1.89	24.20	7
SVM Kernel	3.37	2.48	5.20	9
Efficient Linear Least Square	2.38	1.97	22.95	11
Boosted Trees	1.84	1.49	10.90	153
Bagged Trees	2.07	1.33	8.71	165
Wide Neural Network	0.92	0.98	10.54	10
Bilayered Neural Network	**0.83**	**0.73**	**3.07**	**12**

The algorithm with the lowest RMSE was the Bilayered neural network (BNN) (in bold in Table 3), which is composed of two layers with twenty-five neurons fully connected and a rectified linear unit (ReLU) activation function. This algorithm showed a minimum training time of only 3.07 s, the shortest training time of the algorithms, and a model size of 12 kB.

Figure 5a shows the comparison between the predicted and true responses for the trials used for training. The values cluster near the bisector of the first quadrant, showing low deviations. To better understand the errors made, Figure 5b shows the residuals (difference between true and predicted responses) as a function of true responses. At zero pressure, i.e., for a bending angle of 0°, an error is made with BNN's predictions. These residuals increase as the experimental response increases, but are at most 3.62°. In the entire range of the true response (0–30°), the limited values of the residuals justify the possible use of BNN in the predictions. Thus, these images show that the BNN can predict

responses of the bending angle α as a function of the combinations of the four adopted parameters.

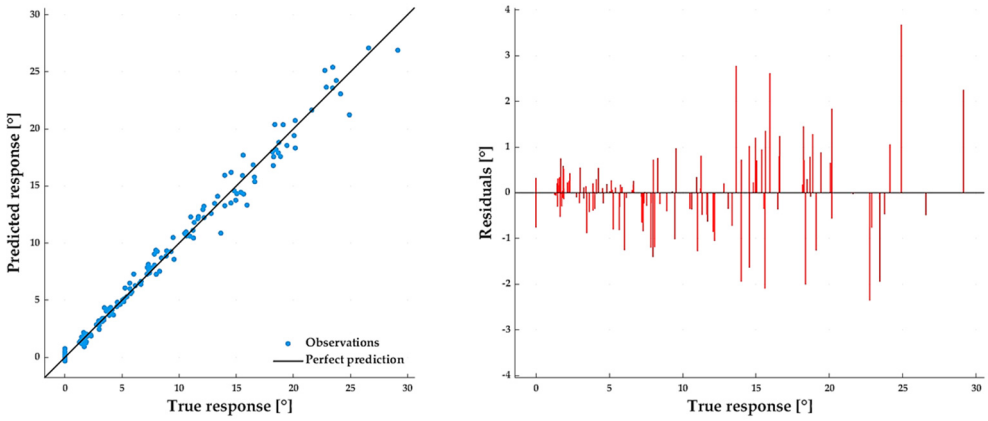

(**a**) (**b**)

Figure 5. Training results for the BNN: (**a**) comparison between predicted and experimental bending angles; (**b**) residual vs. true response.

Turning to the validation, in Figure 6a,b, the plots of the comparison between the predicted and true response and the residuals as a function of the true response are presented. In this case, the residuals are quite constant as a function of the true response, and the error is at most 2.72°. Once again, the BNN can predict the true response with a small absolute error.

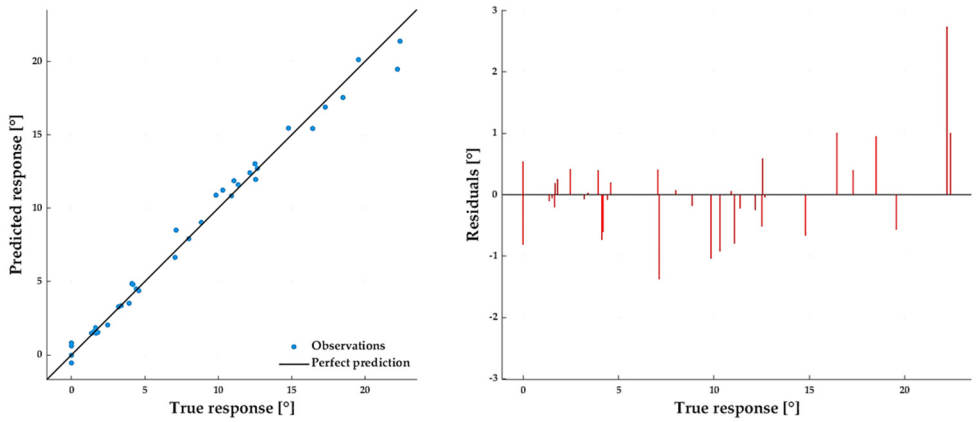

(**a**) (**b**)

Figure 6. Validation results for the BNN: (**a**) comparison between predicted and experimental bending angles; (**b**) residual vs. true response.

4. Experimental Results

4.1. Experimental Tests

Experimental tests were conducted to exclude any overfitting of the BNN on the data adopted for training. Specifically, three new external reinforcements were designed and realized. Reinforcements I and II had the same 115 mm silicone rubber tube as the previous tests, while reinforcement III had a longer one of 180 mm. In this way, it was possible to see if the predictions were acceptable even with different SPA lengths and thus different masses of tubes and reinforcements. Also, the parameter values of the joints, reported in Table 4, differed from those used in constructing the dataset. The parameter N, i.e., the

number of open sectors in each joint, was also added to this analysis. Another advantage of this SPA is the possibility of managing the number of open sectors in each joint to increase or decrease the bending angle. The purpose is to quantify the average absolute error committed between each joint's predicted and experimental bending angles.

Table 4. Parameter values for the external reinforcements used in the experimental test.

Reinforcement	Joint	Parameters			
		L (mm)	R (-)	Θ (°)	N (-)
I	1	5.0	0.65	82	6
II	1	10.0	0.70	70	3
	2	10.0	0.60	70	2
	3	5.0	0.60	70	2
III	1	5.2	0.50	60	2
	2	5.2	0.60	54	2
	3	10.0	0.65	86	2
	4	8.0	0.40	74	2
	5	8.0	0.60	64	2

4.2. Comparison between BNN and RSM

The SPA with reinforcements I and III was mounted vertically, as for the tests conducted for the dataset construction, while the one with reinforcement II was mounted horizontally. This was done to assess whether the predictions could be made by neglecting the gravitational effects of the different SPA assemblies. Figure 7a–i show the deformation states of the three reinforcements at 0.4, 0.8, and 1.2 bar.

The same image analysis followed to construct the dataset was adopted to quantify the experimental joint bending angles (α_{exp}) of each of the three reinforcements. The parameter values of each joint were used to predict the bending angle by both using BNN (α_{BNN}) and a previously identified model with RSM (α_{RSM}) [36]. The experimental and predicted angles of the joints are shown in Table 5. Absolute errors for BNN ($\Delta\alpha_{BNN}$) and RSM ($\Delta\alpha_{RSM}$) were calculated with Equations (4) and (5).

$$\Delta\alpha_{BNN} = \alpha_{exp} - \alpha_{BNN} \quad (4)$$

$$\Delta\alpha_{RSM} = \alpha_{exp} - \alpha_{RSM} \quad (5)$$

The maximum absolute error was 8.20° for BNN and −8.85° for RSM. However, evaluating the average error for reinforcements I, II, and III results in 2.72°, 2.80°, and 2.71° for BNN and 4.55°, 3.91°, and 3.14° for RSM, respectively. These values give further validation to the soft joint design approach by the BNN algorithm. Figure 8 plots the absolute errors as a function of pressure for each of the three reinforcements analyzed to view and compare the results of Table 5 easily. In these figures, the errors have been indicated with $\Delta\alpha$, where the subscripts denote the reinforcement and the joint's number to which it refers, respectively. Figure 8a shows that the error with the BNN (black circles) for reinforcement I seems to have a negative linear trend. However, Figure 8b shows more variability for the absolute errors related to reinforcement II. Only for the predictions of joint 2 (blue circles) is there a negative linear trend, while for joint 1 with the RSM, there is a positive linear trend. Instead, for reinforcement III, analyzed in Figure 8c, the error obtained on joint 2 (blue circles), joint 4 (green circles), and joint 5 (purple triangles) with the BNN remains relatively constant. The error shows a positive linear trend for the RSM prediction on joint 4 (gray stars).

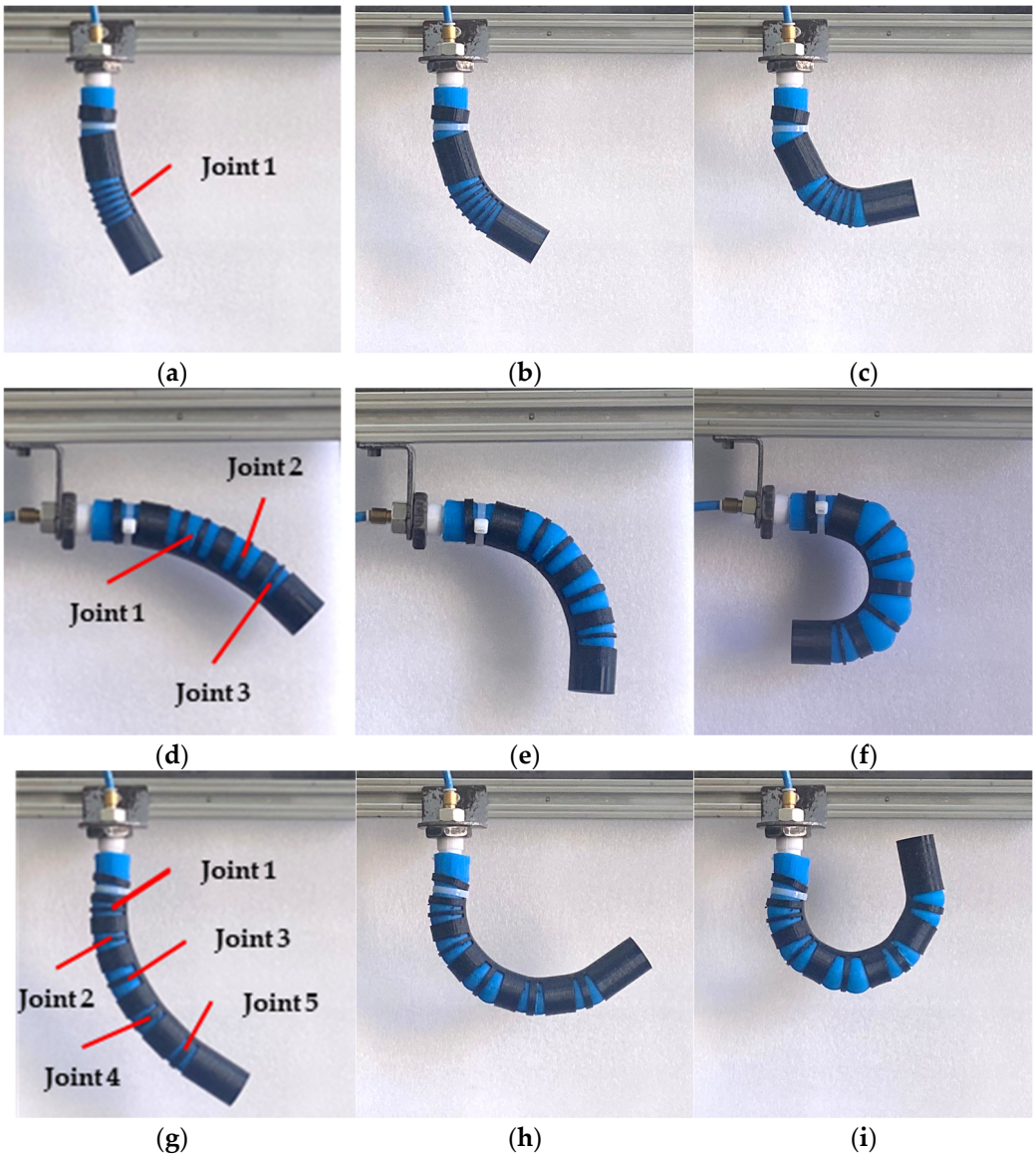

Figure 7. Deformation configurations for reinforcement: (**a**) I at 0.4 bar; (**b**) I at 0.8 bar; (**c**) I at 1.2 bar; (**d**) II at 0.4 bar; (**e**) II at 0.8 bar; (**f**) II at 1.2 bar; (**g**) III at 0.4 bar; (**h**); III at 0.8 bar; (**i**) III 1.2 bar.

Table 5. Experimental angles, predicted angles, and absolute errors for BNN and RSM in experimental tests on reinforcements I, II, and III at 0.4, 0.8, and 1.2 bar. All bending angles and absolute errors are in (°).

Reinforcement	Joint	0.4 bar					0.8 bar					1.2 bar				
		α_{exp}	α_{BNN}	$\Delta\alpha_{BNN}$	α_{RSM}	$\Delta\alpha_{RSM}$	α_{exp}	α_{BNN}	$\Delta\alpha_{BNN}$	α_{RSM}	$\Delta\alpha_{RSM}$	α_{exp}	α_{BNN}	$\Delta\alpha_{BNN}$	α_{RSM}	$\Delta\alpha_{RSM}$
I	1	20.82	18.00	2.82	25.80	−4.98	45.82	45.42	0.40	51.60	−5.78	80.88	85.82	−4.94	78.00	2.88
II	1	15.45	12.66	2.79	24.30	−8.85	44.75	40.49	4.26	49.20	−4.45	73.10	71.51	1.59	74.10	−1.00
	2	10.86	9.22	1.64	16.20	−5.34	24.60	27.53	−2.93	32.40	−7.80	45.56	51.52	−6.06	49.00	−3.54
	3	8.18	8.81	−0.63	9.26	−1.08	16.14	14.36	1.78	18.64	−2.50	27.75	31.30	−3.55	28.12	0.63
III	1	6.57	5.94	0.63	9.40	−2.83	22.76	14.56	8.20	19.00	3.76	30.49	27.63	2.86	28.60	1.89
	2	10.94	5.58	5.36	10.06	0.88	20.87	14.70	6.17	20.24	0.63	33.52	28.09	5.43	30.56	2.96
	3	10.36	7.36	3.00	16.20	−5.84	27.97	23.86	4.11	32.41	−4.44	48.23	48.13	0.10	49.00	−0.77
	4	10.22	9.37	0.85	12.70	−2.48	26.93	27.28	−0.35	25.54	1.39	45.55	44.64	0.91	38.56	6.99
	5	8.50	7.48	1.02	13.54	−5.04	23.77	22.45	1.32	27.24	−3.47	44.89	45.21	−0.32	41.12	3.77

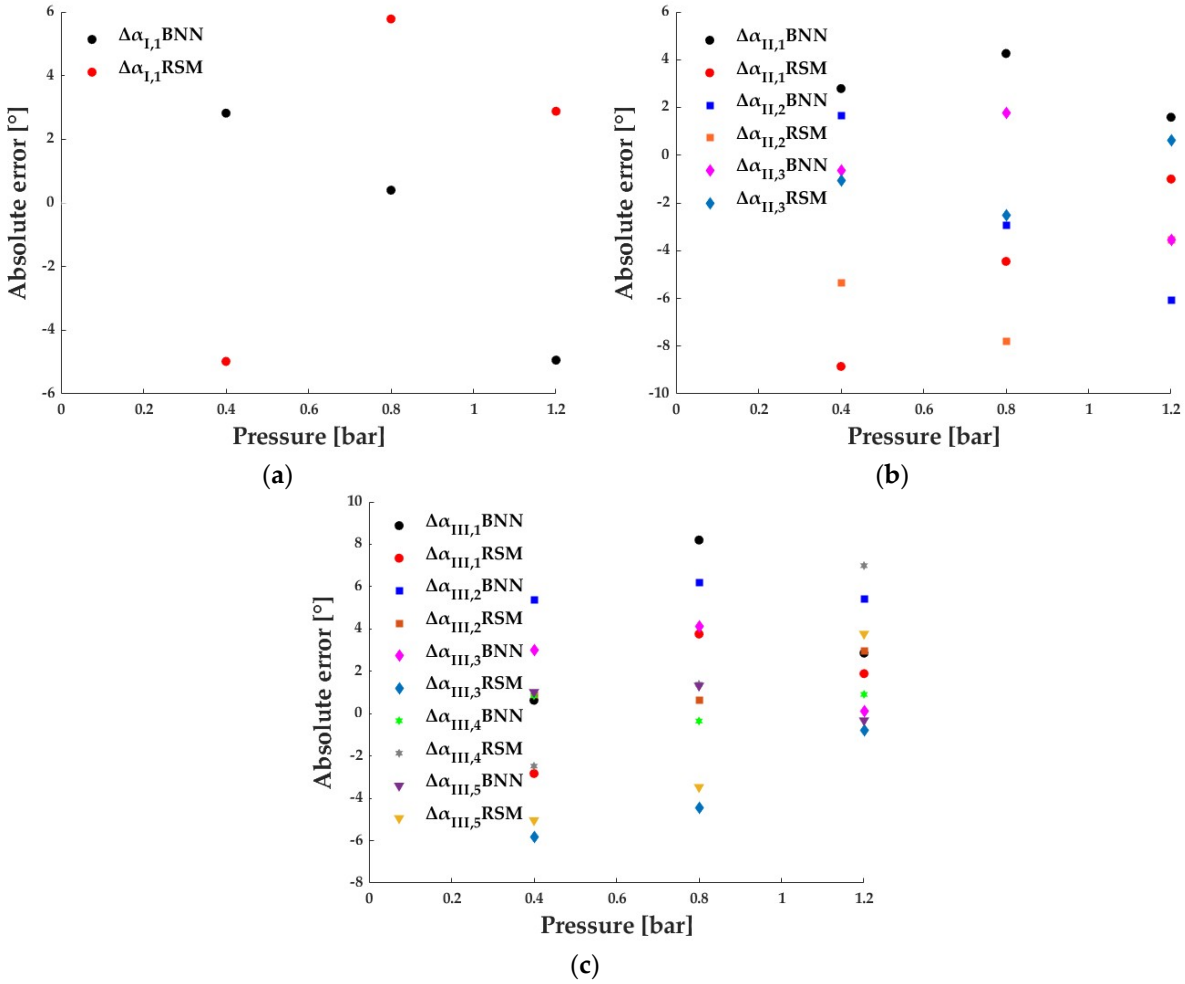

Figure 8. Absolute errors between experimental and predicted bending angles for BNN and RSM as a function of feeding pressure for (**a**) reinforcement I, (**b**) reinforcement II, and (**c**) reinforcement III.

5. Discussion

Characterization conducted with a model-free approach performed better than one with RSM [36]. Both regression algorithms are data-driven and are based on experimental responses. The BNN required a dense campaign of tests to build the Bend dataset, while RSM minimized the number of trials to be conducted. It is true that with the second approach, SPA behavior can be identified with less time and few resources expended, but greater errors are made.

The errors in the experimental tests are described in the previous section, and here the relative percentage errors are quantified. Concerning Table 5 and graphs in Figure 8, in reinforcement I, the bending angles are 20.82° at 0.4 bar, 45.82° at 0.8 bar and 80.88° at 1.2 bar. The absolute errors of 2.82°, 0.40° and 4.94° with the BNN are equal to a relative error of 13.54%, 0.87% and 6.11%, respectively. With the values predicted by RSM, however, the errors rise to 23.92%, 12.61% and 3.56%.

For reinforcement II, the maximum relative errors are for joint 1 at 0.4 bar and for joint 2 at 0.8 bar and 1.2 bar for both algorithms. At these joints and pressures, the bending angles are equal to 15.45°, 24.60° and 16.14°. Specifically, the relative errors are 18.6%, 11.91%, and 13.33% for the BNN and reach 57.28%, 31.71% and 7.79% for RSM.

Reinforcement III, on the other hand, shows a relative error of 48.99% for joint 2 at 0.4 bar, 36.03% at 0.8 bar for joint 1, and finally 16.20% again for joint 2 at 1.2 bar for the BNN. The maximum relative errors with RSM are 59.29% at 0.4 bar for joint 5, 15.87% at 0.8 bar for joint 3, and finally 15.35% for joint 4 at 1.2 bar.

It emerges that the largest errors occur at lower pressures when the SPA bending angles are smaller. This means that for the same absolute error, there is more influence on the relative error at low deflections. However, even when considering relative percentage errors, there were smaller errors with the use of the BNN than RSM.

Making comparisons with other work employing ANNs for characterizing SPAs is quite complex. Indeed, a comparison of algorithm performance would be made on different types of SPAs, such as with and without reinforcement, with different geometries and different materials. In the literature, there are several studies employing ANNs, but the details of the layers or neurons used are often not provided to compare the hyperparameters employed. In addition, the training times are often not specified, and so we were not able to compare the required times either. Also, the input data or dataset responses are different, for example, some consider the spatial position of the SPA tip (X, Y, and Z coordinates) and others the bending angles, as in the present work. The ranges of input parameters can be very different, for example, in terms of actuation pressures, which depend greatly on the materials used. Therefore, a comparison in terms of absolute or relative percentage errors would not be very meaningful.

6. Conclusions

In this work, the bending behavior of an SPA is driven by an external TPU reinforcement with cuts when it is pressurized. The bending angle is managed by the design of the geometric parameters of the cuts and the feeding pressure. Twenty-seven reinforcements with different cut sizes were used to evaluate the influence of the geometrical and functional parameters on the bending angle of the open sector. A total of 189 trials repeated three times were carried out. The average of the three tests was evaluated and inserted as the response of a unique quatern of the chosen input parameters.

Hence, the Bend dataset was realized and adopted to train 14 different regression algorithms: the BNN was the most accurate one, with an RMSE of 0.83° and 0.73° in testing and validation, respectively. To exclude possible overfitting of the BNN, experimental tests were performed on three new reinforcements not employed in the dataset construction. The mean absolute errors for reinforcements I, II, and III were 2.72°, 2.80°, and 2.71° for the BNN and 4.55°, 3.91°, and 3.14° for RSM, respectively.

The BNN demonstrated a significantly lower error than previously obtained by RSM, validating the methodology and highlighting how the application of artificial intelligence techniques can lead to advances in the prediction and design of soft actuators.

It was possible to predict joint bending angles with limited errors even for actuators with different lengths, masses, geometric and functional parameters, numbers of joints, and mounting positions. However, the procedure was very time-consuming, since it required the design and printing of 27 external reinforcements and a total of 567 trials for the creation of the Bend dataset.

Several future developments are possible with the extension of this dataset to other parameters, such as reinforcement inner diameter, reinforcement thickness, or payload applied to the end of the SPA.

Potential applications of the BNN include the mechanical design of soft joints to develop fingers for gripping devices of cobots or in rehabilitative gloves, support legs for robots with locomotion abilities, or reproduce bioinspired structures capable of performing specific bending movements.

Author Contributions: Conceptualization, M.G.A. and N.S.; methodology, M.G.A. and N.S.; software, E.M. and N.S.; validation, E.M. and N.S.; formal analysis, N.S.; investigation, N.S.; data curation, E.M., N.S., M.G.A. and P.B.Z.; writing—original draft preparation, M.G.A. and N.S.; writing—review and editing, M.G.A., P.B.Z., E.M. and N.S.; visualization, P.B.Z., E.M. and N.S.; supervision, M.G.A.; project administration, M.G.A.; funding acquisition, M.G.A. and P.B.Z. All authors have read and agreed to the published version of the manuscript.

Funding: This work was funded by the European Union: NextGenerationEU under the Italian Ministry of University and Research (MUR) National Innovation Ecosystem grant ECS00000041—VITALITY—CUP E13C22001060006.

Institutional Review Board Statement: Not applicable.

Data Availability Statement: The original Bend dataset presented in the study is available at https://www.dropbox.com/scl/fi/06rnxhzgijtq8pl04bd70/Dataset_MATLAB.xlsx?rlkey=x52fnn4b97pr938r188re6f7y&st=clxae2h3&dl=0 (accessed on 10 September 2024).

Conflicts of Interest: The authors declare no conflicts of interest.

References

1. Dzedzickis, A.; Subačiūtė-Žemaitienė, J.; Šutinys, E.; Samukaitė-Bubnienė, U.; Bučinskas, V. Advanced Applications of Industrial Robotics: New Trends and Possibilities. *Appl. Sci.* **2022**, *12*, 135.
2. Laschi, C.; Mazzolai, B.; Cianchetti, M. Soft robotics: Technologies and systems pushing the boundaries of robot abilities. *Sci. Robot.* **2016**, *1*.
3. Kastritsi, T.; Ajoudani, A. A Passive Power-Based Control Strategy for pHRI Tasks With Omni-Directional Robotic Mobile Platforms. *IEEE Robot. Autom. Lett.* **2024**, *9*, 6959–6966.
4. Dragusanu, M.; Marullo, S.; Malvezzi, M.; Achilli, G.M.; Valigi, M.C.; Prattichizzo, D.; Salvietti, G. The DressGripper: A Collaborative Gripper With Electromagnetic Fingertips for Dressing Assistance. *IEEE Robot. Autom. Lett.* **2022**, *7*, 7479–7486.
5. Polsinelli, M.; Di Matteo, A.; Lozzi, D.; Mattei, E.; Mignosi, F.; Nazzicone, L.; Stornelli, V.; Placidi, G. Portable Head-Mounted System for Mobile Forearm Tracking. *Sensors* **2024**, *24*, 2227.
6. Shi, Y.; Wang, T.; Yu, J.; Xiao, S.; Xiong, L.; Yang, L. Virtual Potential Field-Based Motion Planning for Human-Robot Collaboration via Kinesthetically Guided Teleoperation. In Proceedings of the 7th International Conference on Robotics, Control and Automation (ICRCA), Taizhou, China, 5–7 January **2023**; pp. 37–44.
7. Neri, F.; Forlini, M.; Scoccia, C.; Palmieri, G.; Callegari, M. Experimental Evaluation of Collision Avoidance Techniques for Collaborative Robots. *Appl. Sci.* **2023**, *13*, 2944.
8. Antonelli, M.G.; Beomonte Zobel, P.; Manes, C.; Mattei, E.; Stampone, N. Emotional Intelligence for the Decision-Making Process of Trajectories in Collaborative Robotics. *Machines* **2024**, *12*, 113.
9. Heung, K.H.; Lei, T.; Liang, K.; Xu, J.; Seo, J.; Li, H. Quasi-Static Modeling Framework for Soft Bellow-Based Biomimetic Actuators. *Biomimetics* **2024**, *9*, 160.
10. Liu, Y.; Xiao, H.; Hao, T.; Pang, D.; Wang, F.; Liu, S. Dexterous all-soft hand (DASH) with active palm: Multi-functional soft hand beyond grasping. *Smart Mater. Struct.* **2023**, *32*, 125012.
11. Ferraresi, C.; Manuello Bertetto, A.; Mazza, L. Design and Realisation of a Flexible Pneumatic Actuator for Robotics. In Proceedings of the 5th Scandinavian International Conference on Fluid Power, SICFP '97, Linkoping, Sweden, 28–30 May 1997; pp. 29–43.
12. Li, D.; Fan, D.; Zhu, R.; Lei, Q.; Liao, Y.; Yang, X.; Pan, Y.; Wang, Z.; Wu, Y.; Liu, S.; et al. Origami-Inspired Soft Twisting Actuator. *Soft Robot.* **2022**, *10*, 395–409.
13. Antonelli, M.G.; Beomonte Zobel, P.; Sarwar, M.A.; Stampone, N. Seahorse-Tail-Inspired Soft Pneumatic Actuator: Development and Experimental Characterization. *Biomimetics* **2024**, *9*, 264.
14. Li, Y.; Li, Y.; Ren, T.; Xia, J.; Liu, H.; Wu, C.; Lin, S.; Chen, Y. An Untethered Soft Robotic Dog Standing and Fast Trotting with 467 Jointless and Resilient Soft Legs. *Biomimetics* **2023**, *8*, 596.
15. Nodehi, S.E.; Bruzzone, L.; Lalegani Dezaki, M.; Zolfagharian, A.; Bodaghi, M. Porcospino Flex: A Bio-Inspired Single-Track Robot with a 3D-Printed, Flexible, Compliant Vertebral Column. *Robotics* **2024**, *13*, 76.
16. Wang, Z.; Long, Y.; Zhang, Z.; Liu, R.; Wang, H.; Chen, G. Powerful Multidirectional Pneumatic Jumper With Lightweight Fabric Chambers and Buckling-Controllable Elastic Beams. *IEEE Robot. Autom. Lett.* **2024**, *9*, 3347–3354.
17. Fan, J.; Wang, S.; Yu, Q.; Zhu, Y. Swimming Performance of the Frog-Inspired Soft Robot. *Soft Robot.* **2020**, *7*, 615–626.
18. Mendoza, N.; Haghshenas-Jaryani, M. Combined Soft Grasping and Crawling Locomotor Robot for Exterior Navigation of Tubular Structures. *Machines* **2024**, *12*, 157.
19. Meder, F.; Baytekin, B.; Del Dottore, E.; Meroz, Y.; Tauber, F.; Walker, I.; Mazzolai, B. A perspective on plant robotics: From bioispiration to hybrid systems. *Bioinspiration Biomim.* **2023**, *18*, 015006.
20. Marechal, L.; Balland, P.; Lindenroth, L.; Petrou, F.; Kontovounisios, C.; Bello, F. Toward a Common Framework and Database 446 of Materials for Soft Robotics. *Soft Robot.* **2021**, *8*, 284–297.
21. Low, J.H.; Khin, P.M.; Han, Q.Q.; Yao, H.; Teoh, Y.S.; Zeng, Y.; Li, S.; Liu, J.; Liu, Z.; Valdivia y Alvaraldo, P.; et al. Sensorized Reconfigurable Soft Robotic Gripper System for Automated Food Handling. *IEEE/ASME Trans. Mechatron.* **2022**, *27*, 3232–3243.
22. Carello, M.; Ferraresi, C.; Visconte, C. A New Flexible Pneumatic Finger for a Fruit Harvesting Hand. In Proceedings of the 7th International Symposium on Fluid Control, Measurement and Visualization, Sorrento, Italy, 25–28 August **2003**.
23. Antonelli, M.G.; D'Ambrogio, W.; Durante, F. Development of a pneumatic soft actuator as a hand finger for a collaborative robot. In Proceedings of the 2018 2nd International Conference on Mechatronics Systems and Control Engineering (ICMSCE

2018), Amsterdam, The Netherlands, 21–23 February 2018; Association for Computing Machinery: New York, NY, USA, 2018; pp. 67–71.
24. Shintake, J.; Cacucciolo, V.; Floreano, D.; Shea, H. Soft Robotic Grippers. *Adv. Mater.* **2018**, *30*, 1707035.
25. Paterna, M.; De Benedictis, C.; Ferraresi, C. The Research on Soft Pneumatic Actuators in Italy: Design Solutions and Applications. *Actuators* **2022**, *11*, 328.
26. Zhou, J.; Huang, J.; Ma, X.; Lee, A.; Kosuge, K.; Liu, Y.H. Design, Modeling, and Control of Soft Syringes Enabling Two Pumping Modes for Pneumatic Robot Applications. *IEEE/ASME Trans. Mechatron.* **2024**, *29*, 889–901.
27. Kokubu, S.; Wang, Y.; Tortós Vinocour, P.E.; Lu, Y.; Huang, S.; Nishimura, R.; Hsueh, Y.H.; Yu, W. Evaluation of Fiber-Reinforced Modular Soft Actuators for Individualized Soft Rehabilitation Gloves. *Actuators* **2022**, *11*, 84.
28. Antonelli, M.G.; Beomonte Zobel, P.; D'Ambrogio, W.; Durante, F.; Raparelli, T. An Analytical Formula For Designing Mckibben Pneumatic Muscles. *Int. J. Mech. Eng. Technol.* **2018**, *9*, 320–337.
29. Kobayashi, W.; Dohta, S.; Akagi, T.; Ito, K. Analysis and Modeling of Tap-Water/Pneumatic Drive McKibben Type Artificial Muscles. *Int. J. Mech. Eng. Robot. Res.* **2017**, *6*, 463–466.
30. Inada, R.; Tsuruhara, S.; Ito, K. Precise Displacement Control of Tap-Water-Driven Muscle Using Adaptive Model Predictive Control with Hysteresis Compensation. *JFPS Int. J. Fluid Power Syst.* **2022**, *15*, 78–85. https://doi.org/10.5739/jfpsij.15.78.
31. Tsuruhara, S.; Ito, K. Data-Driven Model-Free Adaptive Displacement Control for Tap-Water-Driven Artificial Muscle and Parameter Design Using Virtual Reference Feedback Tuning. *J. Robot. Mechatron.* **2022**, *34*, 664–676.
32. Berthold, R.; Burgner-Kahrs, J.; Wangenheim, M.; Kahms, S. Investigating frictional contact behavior for soft material robot simulations. *Meccanica* **2023**, *58*, 2165–2176.
33. Xavier, M.S.; Tawk, C.D.; Zolfagharian, A.; Pinskier, J.; Howard, D.; Young, T.; Lai, J.; Harrison, S.M.; Yong, Y.K.; Bodaghi, M.; et al. Soft Pneumatic Actuators: A Review of Design, Fabrication, Modeling, Sensing, Control and Applications. *IEEE Access* **2022**, *10*, 59442–59485.
34. Montgomery, D.C. *Design And Analysis of Experiment*, 5th ed.; John Wiley & Son, Inc.: Hoboken, NJ, USA, 2001; ISBN 978-1118-14692-7.
35. Sushant, S.G.; Iftekhar, A.K.; Markus, K. Design of computer experiments: A review. *Comput. Chem. Eng.* **2017**, *106*, 71–95.
36. Antonelli, M.G.; Beomonte Zobel, P.; Stampone, N. Response Surface Methodology for Kinematic Design of Soft Pneumatic Joints: An Application to a Bio-Inspired Scorpion-Tail-Actuator. *Machines* **2024**, *12*, 439.
37. Stampone, N.; Antonelli, M.G. Identification of DOE-based Predictive Model for the Bending Behavior of a Soft Pneumatic Actuator. In *Advances in Italian Mechanism Science. IFToMM Italy*; Mechanism and Machine Science; Springer: Cham, Switzerland, **2024**; Volume 164, p. 52.
38. Lv, Z.; Wu, K.; Zhang, Z.; He, Y. Two-Way FSI Simulation and Experiments for Finger-Like Soft Pneumatic Actuator Under High-Speed Pressurization. *IEEE Robot. Autom. Lett.* **2024**, *9*, 7134–7141.
39. Zournatzis, I.; Kalaitzakis, S.; Polygerinos, P. SoftER: A Spiral Soft Robotic Ejector for Sorting Applications. *IEEE Robot. Autom. Lett.* **2023**, *8*, 7098–7105.
40. García-Samartín, J.F.; Molina-Gómez, R.; Barrientos, A. Model-Free Control of a Soft Pneumatic Segment. *Biomimetics* **2024**, *9*, 127.
41. Elsamanty, M.; Hassaan, M.A.; Orban, M.; Guo, K.; Yang, H.; Abdrabbo, S.; Selmy, M. Soft Pneumatic Muscles: Revolutionizing Human Assistive Devices with Geometric Design and Intelligent Control. *Micromachines* **2023**, *14*, 1431.
42. Li, Y.; Cao, Y.; Jia, F. A Neural Network Based Dynamic Control Method for Soft Pneumatic Actuator with Symmetrical Chambers. *Actuators* **2021**, *10*, 112.
43. Piqué, F.; Kalidindi, H.T.; Fruzzetti, L.; Laschi, C.; Menciassi, A.; Falotico, E. Controlling Soft Robotic Arms Using Continual Learning. *IEEE Robot. Autom. Lett.* **2022**, *7*, 5469–5476.
44. Salem, M.E.M.; Wang, Q.; Xu, M.H. Application of neural network fitting for modeling the pneumatic networks bending soft actuator behavior. *Eng. Res. Express* **2022**, *4*, 015032.
45. Sun, W.; Akashi, N.; Kuniyoshi, Y.; Nakajima, K. Physics-Informed Recurrent Neural Networks for Soft Pneumatic Actuators. *IEEE Robot. Autom. Lett.* **2022**, *7*, 6862–6869.
46. Chiang, C.J.; Chen, Y.C. Neural network fuzzy sliding mode control of pneumatic muscle actuators. *Eng. Appl. Artif. Intell.* **2017**, *65*, 68–86.
47. Chen, C.; Cao, Y.; Chen, X.; Wu, D.; Xiong, C.; Huang, J. A Fused Deep Fuzzy Neural Network Controller and Its Application to Pneumatic Flexible Joint. *IEEE/ASME Trans. Mechatron.* **2023**, *28*, 3214–3225.
48. Acosta, R.; Tafur, J.; Canahuire, R. Self-Tuning Neural Network Controller Based on Fuzzy Logic for Multiple Positions Tracking of a Pneumatic Driven Soft Endoscope Actuator. In Proceedings of the 2024 10th International Conference on Automation, Robotics and Applications (ICARA), Athens, Greece, 22–24 February **2024**; pp. 466–471.
49. Available online: https://www.telematicaricambi.it/iphone-11-pro/954-fotocamera-posteriore-back-camera-apple-iphone-11-pro-flex-a2160-a2217-a2215.html (accessed on 20 August 2024).
50. Available online: https://it.mathworks.com/help/vision/ref/undistortimage.html (accessed on 10 June 2024).
51. Available online: https://it.mathworks.com/help/images/ref/imlocalbrighten.html (accessed on 11 June 2024).
52. Goodfellow, I. *Deep Learning*; MIT Press: Cambridge, MA, USA, 2016.